EUROPEAN ORGANIZATION FOR NUCLEAR RESEARCH

CERN-EP/99-181
December 17, 1999

Measurement of Hadron and Lepton-Pair Production at 130 GeV $< \sqrt{s} <$ 189 GeV at LEP

L3 Collaboration

Abstract

We report on measurements of e^+e^- annihilation into hadrons and lepton pairs. The data have been collected with the L3 detector at LEP at centre-of-mass energies between 130 and 189 GeV. Using a total integrated luminosity of 243.7 pb^{-1}, 25864 hadronic and 8573 lepton-pair events are selected for the measurement of cross sections and leptonic forward-backward asymmetries. The results are in good agreement with Standard Model predictions.

Submitted to *Phys. Lett. B*

1 Introduction

We report on the results of measurements of fermion-pair production above the Z pole, based on data collected using the L3 detector at LEP in 1997 and 1998 at centre-of-mass energies $\sqrt{s} =$ 182.7 GeV and $\sqrt{s} = 188.7$ GeV, respectively. Data corresponding to integrated luminosities of 55.5 pb^{-1} and 176.2 pb^{-1} were collected, leading to much improved statistics compared to our previous publications [1, 2] based on data from 1995 and 1996. In addition, in 1997, small amounts of data, 3.4 pb^{-1} and 3.6 pb^{-1}, were collected at the same centre-of-mass energies as in 1995, 130.0 GeV and 136.1 GeV, respectively. The measurements made on these data samples are combined with those resulting from a re-analysis of the previous data, superseding the results obtained in Reference [1].

In this article we report on measurements of the fermion pair production reactions:

$$\mathrm{e^+e^-} \to \mathrm{hadrons}(\gamma)\,, \quad \mathrm{e^+e^-} \to \mu^+\mu^-(\gamma)\,, \quad \mathrm{e^+e^-} \to \tau^+\tau^-(\gamma)\,, \quad \mathrm{e^+e^-} \to \mathrm{e^+e^-}(\gamma)\,.$$

In these reactions, the (γ) indicates the possible presence of additional photons or low invariant-mass fermion pairs.

For a substantial fraction of the events initial-state radiation, ISR, lowers the initial centre-of-mass energy to an *effective* centre-of-mass energy of the annihilation process, $\sqrt{s'}$. When $\sqrt{s'}$ is close to the Z mass, m_{Z}, the events are classified as radiative returns to the Z. A cut on $\sqrt{s'}$ allows a separation between events at high effective centre-of-mass energies (so-called *high-energy* events), and radiative returns to the Z. Cross sections are measured for all processes and forward-backward asymmetries are measured for the lepton channels and are compared to predictions of the Standard Model [3, 4], both for the high-energy sample and for a larger, *inclusive* sample including also the radiative returns to the Z. Kinematic cuts have been changed with respect to our previous publication [2]. The corresponding results of the cross section and forward-backward asymmetry measurements have been included, with corrections for these changes applied.

Similar studies on the data taken at centre-of-mass energies between 182.7 GeV and 188.7 GeV have been published by other LEP collaborations [5].

2 Analysis Method

The data were collected using the L3 detector described in References [**?**, 6]. For the s-channel processes, the inclusive event sample is defined by requiring $\sqrt{s'} > 60$ GeV for hadronic events and $\sqrt{s'} > 75$ GeV for lepton-pair events, to reduce uncertainties on radiative corrections in extrapolating to low $\sqrt{s'}$ values. The high-energy sample is defined by requiring $\sqrt{s'} > 0.85\sqrt{s}$.

Using the sum of all ISR photon or pair energies, E_γ, and momentum vectors, $\mathbf{P}_\gamma$, the s' value is given by:

$$s' \;=\; s - 2E_\gamma\sqrt{s} + E_\gamma^2 - \mathbf{P}_\gamma^2\,. \tag{1}$$

For most of the events initial-state radiation is along the beam pipe and is not detected. In this case a single photon is assumed to be emitted along the beam axis; its energy is determined from the event kinematics. The $\sqrt{s'}$ value is estimated using Equation 1. The effect of multiple photon and final-state radiation on the $\sqrt{s'}$ calculation has been studied using Monte Carlo programs and is corrected for. The treatment of photons observed in the detector is addressed in the sections describing the individual analyses. Mis-reconstruction of the effective centre-of-mass energy induces a migration of events between the kinematic regions allowed and excluded

by the cut on $\sqrt{s'}$. This is taken into account in the efficiency determination and as an additional background, denominated as ISR contamination.

Bhabha scattering at high energies is dominated by t-channel photon exchange, and hence a cut on s' is less natural. Instead, a cut is applied on the acollinearity angle, ζ, of the final-state e^+ and e^-. In this case, the inclusive and high-energy samples are defined by requiring $\zeta < 120^\circ$ and $\zeta < 25^\circ$, respectively.

Selection efficiencies and backgrounds are determined by Monte Carlo simulations for each centre-of-mass energy using the following event generators: BHLUMI [8] (small-angle Bhabha scattering); PYTHIA [9] ($\mathrm{e^+e^-} \to$ hadrons(γ), ZZ(γ), Zee(γ), Weν(γ)); KORALZ [10] ($\mathrm{e^+e^-} \to \mu^+\mu^-(\gamma)$, $\mathrm{e^+e^-} \to \tau^+\tau^-(\gamma)$); BHAGENE [11] and BHWIDE [12] (large-angle Bhabha scattering); TEEGG [13] ($\mathrm{e^+e^-} \to \mathrm{e^+e^-}\gamma(\gamma)$); GGG [14] ($\mathrm{e^+e^-} \to \gamma\gamma(\gamma)$); PHOJET [15] (hadronic two-photon collisions); DIAG36 [16] ($\mathrm{e^+e^-} \to \mathrm{e^+e^-}\mu^+\mu^-$, $\mathrm{e^+e^-}\tau^+\tau^-$, $\mathrm{e^+e^-e^+e^-}$); FERMISV [17] ($\mathrm{e^+e^-} \to \mathrm{e^+e^-f\bar{f}}$); KORALW [18] ($\mathrm{e^+e^-} \to \mathrm{W^+W^-}(\gamma)$); and EXCALIBUR [19] ($\mathrm{e^+e^-} \to \mathrm{q\bar{q}'e\nu}(\gamma)$, $\mathrm{e^+e^-} \to \mathrm{e^+e^-e^+e^-}$).

The measurements are compared to the predictions of the Standard Model as calculated using the ZFITTER [20] and TOPAZ0 [21] programs with the following parameters [22–26]: $m_\mathrm{Z} = 91.190$ GeV, $\alpha_s(m_\mathrm{Z}^2) = 0.119$, $m_\mathrm{t} = 173.8$ GeV, $\Delta\alpha^{(5)}_\mathrm{had} = 0.02804$, and $m_\mathrm{H} = 150$ GeV. The theoretical uncertainties on the Standard Model predictions are estimated to be below 1% [27] except for the predictions for large angle Bhabha scattering which have an uncertainty of 2% [28].

2.1 Initial-final state interference in *s*-channel processes

In the presence of interference between initial- and final-state radiative corrections, the effective centre-of-mass energy, in contrast to the acollinearity angle, is not well-defined. Moreover, for the s-channel processes, unlike for Bhabha scattering, these contributions are not included in the Monte Carlo samples used to estimate efficiencies. Their effect is expected to be largest for the high-energy $\mu^+\mu^-$ and $\tau^+\tau^-$ samples, affecting cross sections by up to 2% and forward-backward asymmetries by up to 0.02. The following approach is used in the analysis of the s-channel processes.

Cross sections are first determined disregarding this effect. This allows the use of existing Monte Carlo programs without modifications. Corrections are subsequently applied using the Standard Model predictions for the interference contributions, folded with the selection efficiency, ϵ, as a function of the fermion-pair invariant mass, $m_{\mathrm{f\bar{f}}}$, and the scattering angle of the anti-fermion, $\cos\theta$. This leads to an additive correction:

$$\sigma_{\mathrm{f\bar{f}}} \to \sigma_{\mathrm{f\bar{f}}} - \frac{1}{\epsilon}\int_{-1}^{1} \mathrm{d}\cos\theta \int_{\sqrt{s'}}^{\sqrt{s}} \mathrm{d}m_{\mathrm{f\bar{f}}}\, \epsilon(\cos\theta, m_{\mathrm{f\bar{f}}})\, \frac{\mathrm{d}^2\sigma_\mathrm{intf}}{\mathrm{d}\cos\theta\, \mathrm{d}m_{\mathrm{f\bar{f}}}}, \tag{2}$$

where $\mathrm{d}^2\sigma_\mathrm{intf}/\mathrm{d}\cos\theta\, \mathrm{d}m_{\mathrm{f\bar{f}}}$ is the differential interference contribution to the cross section as calculated using the ZFITTER program. The corrections applied range between 0.1% for the hadronic cross section and 1.3% for the leptonic cross sections.

The forward-backward asymmetries for the high-energy samples are obtained as the result of an unbinned maximum-likelihood fit to the polar angular distribution in the Born approximation, to which is added a term representing the differential interference cross section:

$$\frac{1}{\sigma_{\mathrm{f\bar{f}}}}\frac{\mathrm{d}\sigma_{\mathrm{f\bar{f}}}}{\mathrm{d}\cos\theta} = \frac{3}{8}(1+\cos^2\theta) + A_\mathrm{fb}\cos\theta + \frac{1}{\epsilon(\cos\theta)\sigma_{\mathrm{f\bar{f}}}}\int_{\sqrt{s'}}^{\sqrt{s}} \mathrm{d}m_{\mathrm{f\bar{f}}}\, \epsilon(\cos\theta, m_{\mathrm{f\bar{f}}})\, \frac{\mathrm{d}^2\sigma_\mathrm{intf}}{\mathrm{d}\cos\theta\, \mathrm{d}m_{\mathrm{f\bar{f}}}}\,. \tag{3}$$

For the inclusive sample, initial-state radiation distorts the angular distribution, such that the Born approximation in Equation 3 is not appropriate. Instead, the forward-backward asymmetry is obtained directly from the differential cross section and extrapolated to the full solid angle using the ZFITTER program. The differential cross section is corrected analogously to Equation 2. The correction is largest for the asymmetry of the high-energy samples, ranging between 0.004 and 0.010.

2.2 Pair corrections

Besides the emission of ISR photons, also the emission of initial-state pairs can lower the effective centre-of-mass energy of the scattering process. This gives rise to a non-negligible contribution to the inclusive cross section (approximately 1.5% for all s-channels as estimated using the ZFITTER program) when radiative returns to the Z are included in the signal definition. To allow for a proper comparison between experimental measurements and theoretical predictions, these radiative corrections are included in the fermion-pair signal definition.

To calculate the effect of this signal contribution on the overall efficiency, and to estimate the background contributions leading to the same four-fermion final states, events are generated using the DIAG36 program. As this program includes only photon exchange, the events are reweighted to include the effects of Z exchange using the matrix element calculation of the FERMISV program. The selection efficiencies are obtained by combining those estimated from the separate Monte Carlo samples regarded as signal, weighted with their respective cross sections as estimated using the ZFITTER program. As these Monte Carlo programs do not yield a correct description of low-mass hadronic pairs, the efficiency for events with hadronic pairs is taken to be that for the events with lepton pairs. A 20% uncertainty is assigned to this efficiency, resulting in an uncertainty less than 0.2% on the overall efficiency.

Because of the large number of diagrams involved, this approach is less straightforward in the case of Bhabha scattering. Since the relative pair correction is estimated [29] to be significantly smaller than for the s-channel processes, its effect on the selection efficiency is neglected and no correction is applied.

3 Analysis and Results

3.1 Integrated luminosity

The luminosity is measured using small-angle Bhabha scattering [?]. A tight fiducial volume cut, 34 mrad $< \theta <$ 54 mrad and $|90^\circ - \phi| > 11.25^\circ$, $|270^\circ - \phi| > 11.25^\circ$, is imposed on the coordinates of the highest-energy cluster on one side. The highest-energy cluster on the opposite side should be contained in a looser fiducial volume, 32 mrad $< \theta <$ 65 mrad and $|90^\circ - \phi| > 3.75^\circ$, $|270^\circ - \phi| > 3.75^\circ$. This method reduces the theoretical uncertainty.

The experimental systematic uncertainties originate from the event selection criteria, 0.10%, and from the detector geometry, 0.05%. The Monte Carlo statistics result in an uncertainty of 0.07%, yielding a total experimental systematic uncertainty of 0.13%. In addition, a theoretical uncertainty of 0.12% [30] is assigned to the BHLUMI generator, resulting in a total uncertainty of 0.18%.

3.2 $e^+e^- \to$ hadrons(γ)

Event selection

Events are selected by restricting the visible energy, $E_{\rm vis}$, to $0.4 < E_{\rm vis}/\sqrt{s} < 2.0$. The longitudinal energy imbalance must satisfy $|E_{\rm long}|/E_{\rm vis} < 0.7$. The reconstructed energies do not include isolated electromagnetic energy depositions with an energy greater than 10 GeV. These cuts reject most of the background from two-photon collision processes.

In order to reject background originating from lepton pair events, more than 18 calorimetric clusters with an energy exceeding 300 MeV each are requested.

The W-pair production background is reduced by applying the following cuts. Semi-leptonic W-pair decays are rejected by requiring the transverse energy imbalance to be smaller than 0.3 $E_{\rm vis}$. The background from hadronic W-pair decays is reduced by rejecting events with at least four jets each with energy greater than 15 GeV. The jets are obtained using the JADE [31] algorithm with a fixed jet resolution parameter $y_{\rm cut} = 0.01$.

Figure 1a shows the distribution of the visible energy normalised to the centre-of-mass energy for hadronic final state events selected at 189 GeV. The observed peak structure of the signal arises from the high-energy events and from the radiative returns to the Z.

As an additional cross-check, an alternative selection is performed using an artificial neural network technique [32] instead of the cuts described above. The results obtained using the two selection methods are compatible with each other.

To reconstruct the effective centre-of-mass energy, two different methods are used. In the first method, all events are reclustered into two jets using the JADE algorithm. A single photon is assumed to be emitted along the beam axis and to result in a missing momentum vector. From the polar angles of the jets, θ_1 and θ_2, the photon energy is then estimated as:

$$E_\gamma \;=\; \sqrt{s} \cdot \frac{|\sin(\theta_1+\theta_2)|}{\sin\theta_1 + \sin\theta_2 + |\sin(\theta_1+\theta_2)|}\,. \tag{4}$$

The second method uses the clustered jets obtained using the JADE algorithm with a fixed cut, $y_{\rm cut} = 0.01$. A kinematic fit is performed assuming the emission of either zero, one, or two photons along the beam axis. The hypothesis of the smallest number of photons yielding a probability of the kinematic fit larger than 8.5% is used. The cross sections are estimated as the average of the results obtained using the two methods. A systematic uncertainty on the $\sqrt{s'}$ reconstruction, equal to half their difference, is assigned.

For about 10% of the events, a high-energy cluster is detected in the electromagnetic calorimeter. It is selected as described above and is assumed to be a photon. Its energy and momentum are added to the undetected ISR photons. The effective centre-of-mass energy is then calculated using Equation 1.

Figure 2a shows the reconstructed $\sqrt{s'}$ distribution, based on the reconstruction using the jet angles, for hadronic final state events.

Cross section

Selection efficiencies and background contributions are listed, for the $\sqrt{s'}$ reconstruction method using the jet angles, in Table 1. The selected sample contains a background from hadronic two-photon collision processes, W-, Z- and tau-pair production and $e^+e^- \to Ze^+e^-(\gamma)$ events. The two-photon background is estimated by adjusting the Monte Carlo to the data in a two-photon enriched sample.

The numbers of selected events, the total cross sections for the different event samples, and the corresponding statistical and systematic uncertainties are listed in Table 2, together with our previous published measurements [2]. The systematic uncertainties are dominated by the uncertainty on the $\sqrt{s'}$ determination and are correlated between different centre-of-mass energies. In Figure 3 the cross section measurements are shown and compared to the Standard Model predictions.

3.3 $e^+e^- \to \mu^+\mu^-(\gamma)$

Event selection

The event selection for the process $e^+e^- \to \mu^+\mu^-(\gamma)$ follows that of Reference [2]. Two muons are required within the polar angular range $|\cos\theta| < 0.9$. For the data taken at 183 GeV the angular range is restricted to $|\cos\theta| < 0.81$. At least one muon must be measured in the muon spectrometer, and have a momentum greater than 35 GeV. This reduces substantially the background from $e^+e^- \to e^+e^-\mu^+\mu^-$ interactions whilst ensuring a high acceptance for events with hard ISR photons.

Background from cosmic muons is reduced using both scintillation counter time information and the distance of the muon tracks from the beam axis. The number of accepted cosmic muon events is estimated by extrapolating the corresponding sideband distributions to the signal region. Figure 1b shows the distribution of the maximum muon momentum normalised to $E_{\rm beam}$ for events selected at 189 GeV.

The $\sqrt{s'}$ value for each event is determined using Equation 1 assuming the emission of a single ISR photon. In case a photon is detected in the electromagnetic calorimeter it is required to have an energy greater than 15 GeV and an angular separation to the nearest muon of more than 10 degrees. Otherwise the photon is assumed to be emitted along the beam axis and its energy is calculated from the polar angles of the outgoing muons according to Equation 4. The distribution of the reconstructed $\sqrt{s'}$ for events selected at 189 GeV is shown in Figure 2b.

Cross section

Selection efficiencies and background contributions are listed in Table 1. The main background contributions are from the reactions $e^+e^- \to e^+e^-\mu^+\mu^-$, $e^+e^- \to \tau^+\tau^-(\gamma)$ and from W-pair production.

Table 2 summarises the numbers of selected events, the resulting cross sections, and their statistical and systematic uncertainties for the two event samples at the various centre-of-mass energies. The main contributions to the systematic uncertainties originate from the background subtraction and from the acceptance correction. Figure 4 shows the comparison to the Standard Model prediction.

Forward-backward asymmetry

The forward-backward asymmetry is determined using events with two muons with opposite charge and an acollinearity angle smaller than 90 degrees.

For the high-energy sample, the angular distribution of the events is parametrised according to Equation 3. The asymmetry, $A_{\rm fb}$, is determined from an unbinned maximum-likelihood fit of this parametrisation to the data within the fiducial volume. The muon charge is measured as described in Reference [2]. The charge confusion per event, ranging between 0.2% and

0.7%, is taken into account in the fit procedure. The asymmetries for the accepted background contributions are estimated using the same method and are corrected for. The corrections range between 0.045 and 0.059.

For the inclusive event sample the differential cross section is distorted by hard ISR photons. Therefore, $A_{\rm fb}$ is computed directly from the differential cross sections obtained within the fiducial volume. To obtain the asymmetry for the full solid angle an extrapolation factor is calculated using the ZFITTER program. It ranges between 1.10 for the 183 GeV data and 1.03 for the 189 GeV data.

Table 3 summarises the numbers of forward and backward events, the forward-backward asymmetry measurements, and their statistical and systematic uncertainties. The main contributions to the systematic uncertainty are the uncertainties on the backgrounds and on the momentum reconstruction. Figure 4 shows the comparison of the corrected asymmetries to the Standard Model prediction. Table 4 lists the differential cross sections at 183 GeV and 189 GeV, compared to their Standard Model predictions. The 189 GeV distributions are displayed in Figure 5.

3.4 $\mathbf{e^+e^- \to \tau^+\tau^-(\gamma)}$

Event selection

Taus are identified as narrow, low multiplicity jets, containing at least one charged particle. Tau jets are formed by matching the energy depositions in the electromagnetic and hadron calorimeters with tracks in the central tracker and the muon spectrometer. Events containing two jets within the polar angular range $|\cos\theta| < 0.92$ are accepted. The reconstruction of $\sqrt{s'}$ follows the procedure described in Section 3.3 using the polar angles of the two tau jets, requiring at least 10 GeV for observed photons.

Hadronic events are removed by requiring at most 16 calorimetric clusters with an energy exceeding 100 MeV each and at most 9 tracks in the central tracker. Events containing two electrons or two muons are rejected. Electrons are identified by a cluster in the electromagnetic calorimeter with an energy greater than 2.5 GeV and an electromagnetic shower shape, a matched track, and less than 2.5 GeV deposited in the hadron calorimeter. Muons are identified by a track in the muon spectrometer and a minimum-ionising particle signature in the calorimeters. Bhabha events are further rejected by requiring the electromagnetic energy of the highest-energy jet and the other jet to be less than 0.375 $\sqrt{s'}$ and 0.25 $\sqrt{s'}$, respectively. In addition, the acoplanarity of the two jets must be larger than 0.2 degrees.

To reject background from two-photon collision processes the most energetic jet must have an energy greater than 0.24 $E_{\rm beam}$. The distribution of this quantity is shown in Figure 1c for the data taken at 189 GeV. The energy of reconstructed muons is required to be less than 0.4 $\sqrt{s'}$. To reject leptonic final states from W-pair production the acoplanarity of the two tau jets must be less than 10 degrees. Background from cosmic muons is reduced using both scintillation counter information and the distance of the muon tracks from the beam axis. Figure 2c shows the reconstructed $\sqrt{s'}$ distribution for the data taken at 189 GeV.

Cross section

Selection efficiencies and background contaminations are listed in Table 1. The numbers of selected events, as well as the cross sections and corresponding statistical and systematic uncertainties for the different event samples, are listed in Table 2. The systematic uncertainties

originate mainly from uncertainties in the event selection, in particular on the rejection of Bhabha events. Figure 4 shows the comparison to the Standard Model prediction.

Forward-backward asymmetry

For the high-energy sample, the forward-backward asymmetry is determined using an unbinned maximum-likelihood fit of Equation 3 to events with unambiguous charge assignment. The background from other final states and from events with hard ISR photons is corrected for in the fit procedure. The fitted asymmetry is corrected for charge confusion. For the inclusive sample, the forward-backward asymmetry is determined from the differential cross section as described in Section 3.3. For both the inclusive and high-energy samples, the charge confusion per event is estimated, from the data, to be less than 0.5%.

Table 3 lists the number of forward and backward events and the results of the asymmetry measurements. Figure 4 shows the comparison of the measured asymmetries to their Standard Model predictions. Table 4 lists the differential cross sections at 183 GeV and 189 GeV, compared to their Standard Model predictions. The 189 GeV distributions are displayed in Figure 5.

3.5 $e^+e^- \to e^+e^-(\gamma)$

Event selection

Electron candidates are recognised by an energy deposition in the electromagnetic calorimeter with at least 15 associated hits in the central tracking chamber within a three degree azimuthal angular range.

Bhabha events are selected by requiring the two highest energy electron candidates to be contained in the polar angular range $44^\circ < \theta < 136^\circ$, and to have an energy greater than $0.5\,E_{\rm beam}$ and 15 GeV, respectively. Figure 1d shows the energy of the highest energy electron candidate, normalised to the beam energy for events selected at 189 GeV.

The acollinearity angle is calculated from the directions of the two electrons. Its distribution is shown in Figure 2d for events selected at 189 GeV.

Cross section

The selection efficiencies within the fiducial volume and the background contributions are listed in Table 1. The background is dominated by tau-pair production. Table 2 lists the numbers of selected events, and the measured cross sections with their statistical and systematic uncertainties, for the various centre-of-mass energies. The systematic errors are dominated by uncertainties on the event selection. The cross sections are compared to their Standard Model prediction in Figure 6.

Forward-backward asymmetry

The forward-backward asymmetry is extracted from the differential cross section. The selection criteria for electron candidates are tightened to improve the charge determination. The electron direction is obtained from both tracks in the event. The charge confusion probability is determined [22] from the data to be $(2.8 \pm 0.3)\%$ for the 130–136 GeV data, $(4.3 \pm 0.3)\%$ for the 183 GeV data, and $(5.1 \pm 0.2)\%$ for the 189 GeV data, and is corrected for in the determination of the differential cross section. The validity of the method has been verified using a sample

of dimuon events collected at the Z pole in 1995, for which the charge is measured precisely in the muon spectrometer.

Table 3 summarises the numbers of forward and backward events and the asymmetry measurements. The systematic error on the asymmetry measurements is dominated by the uncertainty on the charge confusion. Figure 6 shows the comparison of the measured asymmetries to their Standard Model predictions. Table 5 lists the differential cross sections for the high-energy samples at 183 GeV and 189 GeV, compared to their Standard Model predictions. The 189 GeV distribution is displayed in Figure 7.

4 Summary and Conclusion

Based on an integrated luminosity of 243.7 pb^{-1} collected at centre-of-mass energies between 130.0 GeV and 188.7 GeV, we select 25864 hadronic and 8573 lepton-pair events. The data are used to measure cross sections and leptonic forward-backward asymmetries. The measurements are performed for the inclusive event sample and for the high-energy sample. The results are in good agreement with Standard Model predictions.

Acknowledgements

We wish to congratulate the CERN accelerator divisions for the successful upgrade of the LEP machine and to express our gratitude for the excellent performance of the machine. We acknowledge the effort of the engineers, technicians and support staff who have participated in the construction and maintenance of this experiment.

References

[1] L3 Collab., M. Acciarri *et al.*, Phys. Lett. **B 370** (1996) 195.

[2] L3 Collab., M. Acciarri *et al.*, Phys. Lett. **B 407** (1997) 361.

[3] S.L. Glashow Nucl. Phys. **22** (1961) 579;
S. Weinberg, Phys. Rev. Lett. **19** (1967) 1264;
A. Salam, *Elementary Particle Theory*, ed. N. Svartholm, Stockholm, Almquist & Wiksell (1968) 367.

[4] M. Veltman, Nucl. Phys. **B7** (1968) 637;
G.M. 't Hooft, Nucl. Phys. **B35** (1971) 167;
G.M. 't Hooft and M. Veltman, Nucl. Phys. **B44** (1972) 189; Nucl. Phys. **B50** (1972) 318.

[5] OPAL Collab., G. Abbiendi *et al.*, E. Phys. J. **C 6** (1999) 1; OPAL Collab., G. Abbiendi *et al.*, Tests of the Standard Model and Constraints on New Physics from Measurements of Fermion-pair Production at 189 GeV at LEP, Preprint CERN-EP/99-097, CERN, 1999, accepted by E. Phys. J. C; ALEPH Collab., R. Barate *et al.*, Study of Fermion pair production in e^+e^- collisions at 130-183 GeV, Preprint CERN-EP/99-042, CERN, 1999, submitted to E. Phys. J. C.

[6] L3 Collab., B. Adeva *et al.*, Nucl. Inst. Meth. **A 289** (1990) 35; M. Acciarri *et al.*, Nucl. Inst. Meth. **A 351** (1994) 300; M. Chemarin *et al.*, Nucl. Inst. Meth. **A 349** (1994) 345; A. Adam *et al.*, Nucl. Inst. Meth. **A 383** (1996) 342; G. Basti *et al.*, Nucl. Inst. Meth. **A 374** (1996) 293.

[7] I.C. Brock *et al.*, Nucl. Inst. Meth. **A 381** (1996) 236.

[8] BHLUMI version 4.04 is used.
S. Jadach *et al.*, Comp. Phys. Comm. **70** (1992) 305; Phys. Lett. **B 353** (1995) 349; Phys. Lett. **B 353** (1995) 362; Comp. Phys. Comm. **102** (1997) 229.

[9] T. Sjöstrand, *PYTHIA 5.7 and JETSET 7.4 Physics and Manual*, CERN-TH/7112/93 (1993), revised August 1995; Comp. Phys. Comm. **82** (1994) 74.

[10] KORALZ version 4.01 is used.
S. Jadach, B.F.L. Ward and Z. Wąs, Comp. Phys. Comm. **79** (1994) 503.

[11] BHAGENE version 3 is used.
J.H. Field, Phys. Lett. **B 323** (1994) 432;
J.H. Field and T. Riemann, Comp. Phys. Comm. **94** (1996) 53.

[12] S. Jadach, W. Placzek and B.F.L. Ward, Phys. Lett. **B 390** (1997) 298.

[13] D. Karlen, Nucl. Phys. **B 289** (1987) 23.

[14] F.A. Berends and R. Kleiss, Nucl. Phys. **B 186** (1981) 22.

[15] PHOJET version 1.05 is used.
R. Engel, Z. Phys. **C 66** (1995) 203;
R. Engel and J. Ranft, Phys. Rev. **D 54** (1996) 4244.

[16] F.A. Berends, P.H. Daverveldt and R. Kleiss, Nucl. Phys. **B 253** (1985) 441.

[17] J. Hilgart, R. Kleiss and F. Le Diberder, Comp. Phys. Comm. **75** (1993) 191.

[18] KORALW version 1.21 is used.
M. Skrzypek, S. Jadach, W. Placzek and Z. Wąs, Comp. Phys. Comm. **94** (1996) 216;
M. Skrzypek, S. Jadach, M. Martinez, W. Placzek and Z. Wąs, Phys. Lett. **B 372** (1996) 289.

[19] F.A. Berends, R. Kleiss and R. Pittau, Nucl. Phys. **B 424** (1994) 308; Nucl. Phys. **B 426** (1994) 344; Nucl. Phys. (Proc. Suppl.) **B 37** (1994) 163; Phys. Lett. **B 335** (1994) 490; Comp. Phys. Comm. **83** (1994) 141.

[20] ZFITTER version 6.21 is used.
D. Bardin *et al.*, Preprint hep-ph/9908433; Z. Phys. **C 44** (1989) 493; Nucl. Phys. **B 351** (1991) 1; Phys. Lett. **B 255** (1991) 290. For the comparison with our measurements, the following ZFITTER flags have been changed from their default values: `FINR` = 0, `INTF` = 0, and `BOXD` = 2.

[21] TOPAZ0 version 4.4 is used.
G. Montagna, O. Nicrosini, G. Passarino, F. Piccinini and R. Pittau, Nucl. Phys. **B401** (1993) 3; Comp. Phys. Comm. **76** (1993) 328.

[22] L3 Collab., M. Acciarri *et al.*, Z. Phys. **C 62** (1994) 551.

[23] L3 Collab., O. Adriani *et al.*, Physics Reports **236** (1993) 1.

[24] Particle Data Group, C. Caso *et al.*, E. Phys. J. **C 3** (1998) 1.

[25] S. Eidelman and F. Jegerlehner, Z. Phys. **C 67** (1995) 585.

[26] CDF Collab., F. Abe *et al.*, Phys. Rev. Lett. **74** (1995) 2626; CDF Collab., F. abe *et al.*, Phys. Rev. Lett. **82** (1999) 2808; DØ Collab., S. Abachi *et al.*, Phys. Rev. Lett. **74** (1995) 2632; we use the average top mass as given in Reference [24].

[27] D. Bardin, private communication.

[28] H. Anlauf *et al.*, in Physics at LEP2, Vol. 2, ed. T. Sjöstrand G. Altarelli and F. Zwirner, (Yellow Report: CERN 96-01, 1996), p. 229.

[29] G. Passarino, private communication.

[30] B.F.L. Ward, S. Jadach, M. Melles and S.A. Yost, Phys. Lett. **B 450** (1999) 262.

[31] JADE Collab., W. Bartel *et al.*, Z. Phys. **C 33** (1986) 23;
JADE Collab., S. Bethke *et al.*, Phys. Lett. **B 213** (1988) 235.

[32] M. von der Mey, Messung der Reaktion $e^+e^- \to q\bar{q}(\gamma)$ mit dem L3-Detektor bei LEP, Ph.D. thesis, RWTH Aachen, 1999.

The L3 Collaboration:

M.Acciarri,[26] P.Achard,[19] O.Adriani,[16] M.Aguilar-Benitez,[25] J.Alcaraz,[25] G.Alemanni,[22] J.Allaby,[17] A.Aloisio,[28] M.G.Alviggi,[28] G.Ambrosi,[19] H.Anderhub,[47] V.P.Andreev,[6,36] T.Angelescu,[12] F.Anselmo,[9] A.Arefiev,[27] T.Azemoon,[3] T.Aziz,[10] P.Bagnaia,[35] L.Baksay,[42] A.Balandras,[4] R.C.Ball,[3] S.Banerjee,[10] Sw.Banerjee,[10] A.Barczyk,[47,45] R.Barillère,[17] L.Barone,[35] P.Bartalini,[22] M.Basile,[9] R.Battiston,[32] A.Bay,[22] F.Becattini,[16] U.Becker,[14] F.Behner,[47] L.Bellucci,[16] J.Berdugo,[25] P.Berges,[14] B.Bertucci,[32] B.L.Betev,[47] S.Bhattacharya,[10] M.Biasini,[32] A.Biland,[47] J.J.Blaising,[4] S.C.Blyth,[33] G.J.Bobbink,[2] A.Böhm,[1] L.Boldizsar,[13] B.Borgia,[35] D.Bourilkov,[47] M.Bourquin,[19] S.Braccini,[19] J.G.Branson,[38] V.Brigljevic,[47] F.Brochu,[4] A.Buffini,[16] A.Buijs,[43] J.D.Burger,[14] W.J.Burger,[32] A.Button,[3] X.D.Cai,[14] M.Campanelli,[47] M.Capell,[14] G.Cara Romeo,[9] G.Carlino,[28] A.M.Cartacci,[16] J.Casaus,[25] G.Castellini,[16] F.Cavallari,[35] N.Cavallo,[28] C.Cecchi,[32] M.Cerrada,[25] F.Cesaroni,[23] M.Chamizo,[19] Y.H.Chang,[49] U.K.Chaturvedi,[18] M.Chemarin,[24] A.Chen,[49] G.Chen,[7] G.M.Chen,[7] H.F.Chen,[20] H.S.Chen,[7] G.Chiefari,[28] L.Cifarelli,[37] F.Cindolo,[9] C.Civinini,[16] I.Clare,[14] R.Clare,[14] G.Coignet,[4] A.P.Colijn,[2] N.Colino,[25] S.Costantini,[5] F.Cotorobai,[12] B.Cozzoni,[9] B.de la Cruz,[25] A.Csilling,[13] S.Cucciarelli,[32] T.S.Dai,[14] J.A.van Dalen,[30] R.D'Alessandro,[16] R.de Asmundis,[28] P.Déglon,[19] A.Degré,[4] K.Deiters,[45] D.della Volpe,[28] P.Denes,[34] F.DeNotaristefani,[35] A.De Salvo,[47] M.Diemoz,[35] D.van Dierendonck,[2] F.Di Lodovico,[47] C.Dionisi,[35] M.Dittmar,[47] A.Dominguez,[38] A.Doria,[28] M.T.Dova,[18,♯] D.Duchesneau,[4] D.Dufournaud,[4] P.Duinker,[2] I.Duran,[39] H.El Mamouni,[24] A.Engler,[33] F.J.Eppling,[14] F.C.Erné,[2] P.Extermann,[19] M.Fabre,[45] R.Faccini,[35] M.A.Falagan,[25] S.Falciano,[35,17] A.Favara,[17] J.Fay,[24] O.Fedin,[36] M.Felcini,[47] T.Ferguson,[33] F.Ferroni,[35] H.Fesefeldt,[1] E.Fiandrini,[32] J.H.Field,[19] F.Filthaut,[17] P.H.Fisher,[14] I.Fisk,[38] G.Forconi,[14] L.Fredj,[19] K.Freudenreich,[47] C.Furetta,[26] Yu.Galaktionov,[27,14] S.N.Ganguli,[10] P.Garcia-Abia,[5] M.Gataullin,[31] S.S.Gau,[11] S.Gentile,[35,17] N.Gheordanescu,[12] S.Giagu,[35] Z.F.Gong,[20] G.Grenier,[24] O.Grimm,[47] M.W.Gruenewald,[8] M.Guida,[37] R.van Gulik,[2] V.K.Gupta,[34] A.Gurtu,[10] L.J.Gutay,[44] D.Haas,[5] A.Hasan,[29] D.Hatzifotiadou,[9] T.Hebbeker,[8] A.Hervé,[17] P.Hidas,[13] J.Hirschfelder,[33] H.Hofer,[47] G. Holzner,[47] H.Hoorani,[33] S.R.Hou,[49] I.Iashvili,[46] B.N.Jin,[7] L.W.Jones,[3] P.de Jong,[2] I.Josa-Mutuberría,[25] R.A.Khan,[18] M.Kaur,[18,◇] M.N.Kienzle-Focacci,[19] D.Kim,[35] D.H.Kim,[41] J.K.Kim,[41] S.C.Kim,[41] J.Kirkby,[17] D.Kiss,[13] W.Kittel,[30] A.Klimentov,[14,27] A.C.König,[30] A.Kopp,[46] V.Koutsenko,[14,27] M.Kräber,[47] R.W.Kraemer,[33] W.Krenz,[1] A.Krüger,[46] A.Kunin,[14,27] P.Ladron de Guevara,[25] I.Laktineh,[24] G.Landi,[16] K.Lassila-Perini,[47] M.Lebeau,[17] A.Lebedev,[14] P.Lebrun,[24] P.Lecomte,[47] P.Lecoq,[17] P.Le Coultre,[47] H.J.Lee,[8] J.M.Le Goff,[17] R.Leiste,[46] E.Leonardi,[35] P.Levtchenko,[36] C.Li,[20] S.Likhoded,[46] C.H.Lin,[49] W.T.Lin,[49] F.L.Linde,[2] L.Lista,[28] Z.A.Liu,[7] W.Lohmann,[46] E.Longo,[35] Y.S.Lu,[7] K.Lübelsmeyer,[1] C.Luci,[17,35] D.Luckey,[14] L.Lugnier,[24] L.Luminari,[35] W.Lustermann,[47] W.G.Ma,[20] M.Maity,[10] L.Malgeri,[17] A.Malinin,[17] C.Maña,[25] D.Mangeol,[30] P.Marchesini,[47] G.Marian,[15] J.P.Martin,[24] F.Marzano,[35] G.G.G.Massaro,[2] K.Mazumdar,[10] R.R.McNeil,[6] S.Mele,[17] L.Merola,[28] M.Meschini,[16] W.J.Metzger,[30] M.von der Mey,[1] A.Mihul,[12] H.Milcent,[17] G.Mirabelli,[35] J.Mnich,[17] G.B.Mohanty,[10] P.Molnar,[8] B.Monteleoni,[16,†] T.Moulik,[10] G.S.Muanza,[24] F.Muheim,[19] A.J.M.Muijs,[2] M.Musy,[35] M.Napolitano,[28] F.Nessi-Tedaldi,[47] H.Newman,[31] T.Niessen,[1] A.Nisati,[35] H.Nowak,[46] Y.D.Oh,[41] G.Organtini,[35] A.Oulianov,[27] C.Palomares,[25] D.Pandoulas,[1] S.Paoletti,[35,17] P.Paolucci,[28] R.Paramatti,[35] H.K.Park,[33] I.H.Park,[41] G.Pascale,[35] G.Passaleva,[17] S.Patricelli,[28] T.Paul,[11] M.Pauluzzi,[32] C.Paus,[17] F.Pauss,[47] M.Pedace,[35] S.Pensotti,[26] D.Perret-Gallix,[4] B.Petersen,[30] D.Piccolo,[28] F.Pierella,[9] M.Pieri,[16] P.A.Piroué,[34] E.Pistolesi,[26] V.Plyaskin,[27] M.Pohl,[19] V.Pojidaev,[27,16] H.Postema,[14] J.Pothier,[17] N.Produit,[19] D.O.Prokofiev,[44] D.Prokofiev,[36] J.Quartieri,[37] G.Rahal-Callot,[47,17] M.A.Rahaman,[10] P.Raics,[15] N.Raja,[10] R.Ramelli,[47] P.G.Rancoita,[26] A.Raspereza,[46] G.Raven,[38] P.Razis,[29] D.Ren,[47] M.Rescigno,[35] S.Reucroft,[11] T.van Rhee,[43] S.Riemann,[46] K.Riles,[3] A.Robohm,[47] J.Rodin,[42] B.P.Roe,[3] L.Romero,[25] A.Rosca,[8] S.Rosier-Lees,[4] J.A.Rubio,[17] D.Ruschmeier,[8] H.Rykaczewski,[47] S.Saremi,[6] S.Sarkar,[35] J.Salicio,[17] E.Sanchez,[17] M.P.Sanders,[30] M.E.Sarakinos,[21] C.Schäfer,[17] V.Schegelsky,[36] S.Schmidt-Kaerst,[1] D.Schmitz,[1] H.Schopper,[48] D.J.Schotanus,[30] G.Schwering,[1] C.Sciacca,[28] D.Sciarrino,[19] A.Seganti,[9] L.Servoli,[32] S.Shevchenko,[31] N.Shivarov,[40] V.Shoutko,[27] E.Shumilov,[27] A.Shvorob,[31] T.Siedenburg,[1] D.Son,[41] B.Smith,[33] P.Spillantini,[16] M.Steuer,[14] D.P.Stickland,[34] A.Stone,[6] H.Stone,[34,†] B.Stoyanov,[40] A.Straessner,[1] K.Sudhakar,[10] G.Sultanov,[18] L.Z.Sun,[20] H.Suter,[47] J.D.Swain,[18] Z.Szillasi,[42,¶] T.Sztaricskai,[42,¶] X.W.Tang,[7] L.Tauscher,[5] L.Taylor,[11] C.Timmermans,[30] Samuel C.C.Ting,[14] S.M.Ting,[14] S.C.Tonwar,[10] J.Tóth,[13] C.Tully,[17] K.L.Tung,[7] Y.Uchida,[14] J.Ulbricht,[47] E.Valente,[35] G.Vesztergombi,[13] I.Vetlitsky,[27] D.Vicinanza,[37] G.Viertel,[47] S.Villa,[11] M.Vivargent,[4] S.Vlachos,[5] I.Vodopianov,[36] H.Vogel,[33] H.Vogt,[46] I.Vorobiev,[27] A.A.Vorobyov,[36] A.Vorvolakos,[29] M.Wadhwa,[5] W.Wallraff,[1] M.Wang,[14] X.L.Wang,[20] Z.M.Wang,[20] A.Weber,[1] M.Weber,[1] P.Wienemann,[1] H.Wilkens,[30] S.X.Wu,[14] S.Wynhoff,[17] L.Xia,[31] Z.Z.Xu,[20] B.Z.Yang,[20] C.G.Yang,[7] H.J.Yang,[7] M.Yang,[7] J.B.Ye,[20] S.C.Yeh,[50] An.Zalite,[36] Yu.Zalite,[36] Z.P.Zhang,[20] G.Y.Zhu,[7] R.Y.Zhu,[31] A.Zichichi,[9,17,18] G.Zilizi,[42,¶] M.Zöller.[1]

1 I. Physikalisches Institut, RWTH, D-52056 Aachen, FRG[§]
III. Physikalisches Institut, RWTH, D-52056 Aachen, FRG[§]
2 National Institute for High Energy Physics, NIKHEF, and University of Amsterdam, NL-1009 DB Amsterdam, The Netherlands
3 University of Michigan, Ann Arbor, MI 48109, USA
4 Laboratoire d'Annecy-le-Vieux de Physique des Particules, LAPP,IN2P3-CNRS, BP 110, F-74941 Annecy-le-Vieux CEDEX, France
5 Institute of Physics, University of Basel, CH-4056 Basel, Switzerland
6 Louisiana State University, Baton Rouge, LA 70803, USA
7 Institute of High Energy Physics, IHEP, 100039 Beijing, China[△]
8 Humboldt University, D-10099 Berlin, FRG[§]
9 University of Bologna and INFN-Sezione di Bologna, I-40126 Bologna, Italy
10 Tata Institute of Fundamental Research, Bombay 400 005, India
11 Northeastern University, Boston, MA 02115, USA
12 Institute of Atomic Physics and University of Bucharest, R-76900 Bucharest, Romania
13 Central Research Institute for Physics of the Hungarian Academy of Sciences, H-1525 Budapest 114, Hungary[‡]
14 Massachusetts Institute of Technology, Cambridge, MA 02139, USA
15 KLTE-ATOMKI, H-4010 Debrecen, Hungary[¶]
16 INFN Sezione di Firenze and University of Florence, I-50125 Florence, Italy
17 European Laboratory for Particle Physics, CERN, CH-1211 Geneva 23, Switzerland
18 World Laboratory, FBLJA Project, CH-1211 Geneva 23, Switzerland
19 University of Geneva, CH-1211 Geneva 4, Switzerland
20 Chinese University of Science and Technology, USTC, Hefei, Anhui 230 029, China[△]
21 SEFT, Research Institute for High Energy Physics, P.O. Box 9, SF-00014 Helsinki, Finland
22 University of Lausanne, CH-1015 Lausanne, Switzerland
23 INFN-Sezione di Lecce and Universitá Degli Studi di Lecce, I-73100 Lecce, Italy
24 Institut de Physique Nucléaire de Lyon, IN2P3-CNRS,Université Claude Bernard, F-69622 Villeurbanne, France
25 Centro de Investigaciones Energéticas, Medioambientales y Tecnologícas, CIEMAT, E-28040 Madrid, Spain[♭]
26 INFN-Sezione di Milano, I-20133 Milan, Italy
27 Institute of Theoretical and Experimental Physics, ITEP, Moscow, Russia
28 INFN-Sezione di Napoli and University of Naples, I-80125 Naples, Italy
29 Department of Natural Sciences, University of Cyprus, Nicosia, Cyprus
30 University of Nijmegen and NIKHEF, NL-6525 ED Nijmegen, The Netherlands
31 California Institute of Technology, Pasadena, CA 91125, USA
32 INFN-Sezione di Perugia and Universitá Degli Studi di Perugia, I-06100 Perugia, Italy
33 Carnegie Mellon University, Pittsburgh, PA 15213, USA
34 Princeton University, Princeton, NJ 08544, USA
35 INFN-Sezione di Roma and University of Rome, "La Sapienza", I-00185 Rome, Italy
36 Nuclear Physics Institute, St. Petersburg, Russia
37 University and INFN, Salerno, I-84100 Salerno, Italy
38 University of California, San Diego, CA 92093, USA
39 Dept. de Fisica de Particulas Elementales, Univ. de Santiago, E-15706 Santiago de Compostela, Spain
40 Bulgarian Academy of Sciences, Central Lab. of Mechatronics and Instrumentation, BU-1113 Sofia, Bulgaria
41 Center for High Energy Physics, Adv. Inst. of Sciences and Technology, 305-701 Taejon, Republic of Korea
42 University of Alabama, Tuscaloosa, AL 35486, USA
43 Utrecht University and NIKHEF, NL-3584 CB Utrecht, The Netherlands
44 Purdue University, West Lafayette, IN 47907, USA
45 Paul Scherrer Institut, PSI, CH-5232 Villigen, Switzerland
46 DESY, D-15738 Zeuthen, FRG
47 Eidgenössische Technische Hochschule, ETH Zürich, CH-8093 Zürich, Switzerland
48 University of Hamburg, D-22761 Hamburg, FRG
49 National Central University, Chung-Li, Taiwan, China
50 Department of Physics, National Tsing Hua University, Taiwan, China
§ Supported by the German Bundesministerium für Bildung, Wissenschaft, Forschung und Technologie
‡ Supported by the Hungarian OTKA fund under contract numbers T019181, F023259 and T024011.
¶ Also supported by the Hungarian OTKA fund under contract numbers T22238 and T026178.
♭ Supported also by the Comisión Interministerial de Ciencia y Tecnología.
♯ Also supported by CONICET and Universidad Nacional de La Plata, CC 67, 1900 La Plata, Argentina.
♢ Also supported by Panjab University, Chandigarh-160014, India.
△ Supported by the National Natural Science Foundation of China.
† Deceased.

$\sqrt{s}$ (GeV)	inclusive (%) 130.0	136.1	182.7	188.7	high energy (%) 130.0	136.1	182.7	188.7
$e^+e^- \to$ hadrons(γ)								
Selection Efficiency	97.4	97.2	90.0	89.2	93.7	93.8	88.2	88.1
Two Photon Background	1.8	1.8	2.5	2.8	1.4	1.8	1.8	1.9
W^+W^- Background	—	—	4.4	5.2	—	—	6.9	8.1
Other Background	0.2	0.2	1.3	1.4	0.3	0.4	0.9	1.1
ISR Contamination	0.2	0.1	0.2	0.2	17.7	17.0	11.4	11.2
$e^+e^- \to \mu^+\mu^-(\gamma)$								
Selection Efficiency	68.6	65.9	47.4	61.4	78.8	73.8	63.9	75.4
Two Photon Background	2.0	2.8	4.8	10.0	0.8	1.5	1.8	2.9
W^+W^- Background	—	—	0.7	2.9	—	—	0.5	2.5
Cosmic Background	0.9	1.1	2.0	0.5	0.9	2.4	1.8	0.4
Other Background	0.4	0.7	2.8	2.8	0.2	0.1	1.2	1.3
ISR Contamination	0.4	0.4	0.4	0.3	8.0	6.7	4.1	4.2
$e^+e^- \to \tau^+\tau^-(\gamma)$								
Selection Efficiency	45.9	38.7	35.2	34.8	51.0	45.0	47.2	47.3
Two Photon Background	2.3	2.1	7.2	7.4	1.3	1.2	2.6	2.2
Other Background	3.0	5.5	4.8	7.2	2.2	3.7	3.7	5.8
ISR Contamination	0.5	0.5	0.5	0.4	7.6	7.3	5.2	5.2
$e^+e^- \to e^+e^-(\gamma)$								
Selection Efficiency	97.9	97.6	96.4	97.5	98.0	97.6	95.9	97.1
$\tau^+\tau^-$ Background	1.3	1.5	1.3	1.3	1.1	1.4	1.3	1.3
Other Background	0.6	1.1	1.2	1.3	0.6	0.5	0.7	0.6

Table 1: Selection efficiencies and background fractions for the inclusive and the high-energy event samples of the reactions $e^+e^- \to$ hadrons(γ), $e^+e^- \to \mu^+\mu^-(\gamma)$, $e^+e^- \to \tau^+\tau^-(\gamma)$ and $e^+e^- \to e^+e^-(\gamma)$. For Bhabha scattering the selection efficiencies are given for $44^\circ < \theta < 136^\circ$.

		inclusive			high energy		
$\sqrt{s}$ (GeV)	$\mathcal{L}$ (pb^{-1})	$N_{\rm sel}$	σ (pb)	$\sigma_{\rm SM}$ (pb)	$N_{\rm sel}$	σ (pb)	$\sigma_{\rm SM}$ (pb)
$e^+e^- \to$ hadrons(γ)							
130.0	6.1	1972	$326.0 \pm 7.5 \pm 1.9$	329.5	632	$84.2 \pm 4.4 \pm 1.0$	83.5
136.1	5.8	1571	$274.4 \pm 7.0 \pm 1.8$	272.0	460	$66.6 \pm 3.9 \pm 0.8$	66.9
161.3	10.0	1542	$152.5 \pm 4.1 \pm 1.7$	151.8	423	$37.3 \pm 2.2 \pm 0.7$	35.4
172.3	8.5	1064	$121.2 \pm 4.1 \pm 1.3$	124.5	248	$28.2 \pm 2.2 \pm 0.6$	28.8
182.7	54.9	5626	$105.2 \pm 1.5 \pm 0.5$	105.7	1505	$24.7 \pm 0.8 \pm 0.4$	24.3
188.7	173.4	16695	$98.2 \pm 0.8 \pm 0.4$	96.9	4517	$23.1 \pm 0.4 \pm 0.3$	22.2
$e^+e^- \to \mu^+\mu^-(\gamma)$							
130.1	6.1	91	$21.0 \pm 2.3 \pm 1.0$	20.9	44	$8.2 \pm 1.4 \pm 0.2$	8.5
136.1	5.9	70	$17.5 \pm 2.2 \pm 0.9$	17.8	33	$6.9 \pm 1.4 \pm 0.3$	7.3
161.3	10.9	94	$12.5 \pm 1.4 \pm 0.5$	10.9	41	$4.59 \pm 0.84 \pm 0.18$	4.70
172.1	10.2	67	$9.2 \pm 1.3 \pm 0.4$	9.2	32	$3.60 \pm 0.75 \pm 0.14$	4.00
182.7	50.5	197	$7.34 \pm 0.59 \pm 0.27$	7.90	111	$3.09 \pm 0.33 \pm 0.14$	3.47
188.7	167.4	893	$7.28 \pm 0.29 \pm 0.19$	7.29	420	$2.92 \pm 0.16 \pm 0.06$	3.22
$e^+e^- \to \tau^+\tau^-(\gamma)$							
130.1	6.1	66	$22.1 \pm 2.9 \pm 0.5$	20.9	35	$9.8 \pm 1.9 \pm 0.3$	8.5
136.1	5.9	43	$17.1 \pm 2.8 \pm 0.5$	17.8	23	$7.5 \pm 1.8 \pm 0.3$	7.3
161.3	9.8	45	$10.4 \pm 2.0 \pm 0.7$	10.9	25	$4.6 \pm 1.1 \pm 0.3$	4.7
172.1	9.7	45	$11.0 \pm 2.0 \pm 0.8$	9.2	23	$4.3 \pm 1.1 \pm 0.3$	4.0
182.7	55.5	174	$7.77 \pm 0.68 \pm 0.17$	7.89	108	$3.62 \pm 0.40 \pm 0.06$	3.47
188.7	176.8	527	$7.27 \pm 0.37 \pm 0.17$	7.28	309	$3.18 \pm 0.21 \pm 0.07$	3.22
$e^+e^- \to e^+e^-(\gamma)$							
130.1	6.1	312	$51.1 \pm 2.9 \pm 0.2$	56.5	274	$45.0 \pm 2.7 \pm 0.2$	49.7
136.1	5.8	281	$49.3 \pm 2.9 \pm 0.2$	50.9	248	$43.6 \pm 2.8 \pm 0.2$	45.4
161.3	10.2	337	$34.0 \pm 1.9 \pm 1.0$	35.1	289	$31.1 \pm 1.8 \pm 0.9$	32.4
172.3	8.8	256	$30.8 \pm 1.9 \pm 0.9$	30.3	207	$26.7 \pm 1.8 \pm 0.8$	28.3
182.7	55.3	1506	$27.6 \pm 0.7 \pm 0.2$	26.7	1385	$25.6 \pm 0.7 \pm 0.1$	25.0
188.7	175.9	4413	$25.1 \pm 0.4 \pm 0.1$	24.9	4097	$23.5 \pm 0.4 \pm 0.1$	23.4

Table 2: Number of selected events, $N_{\rm sel}$, measured cross sections, σ, statistical errors and systematic errors and the Standard Model predictions, $\sigma_{\rm SM}$, of the reactions $e^+e^- \to$ hadrons(γ), $e^+e^- \to \mu^+\mu^-(\gamma)$, $e^+e^- \to \tau^+\tau^-(\gamma)$ and $e^+e^- \to e^+e^-(\gamma)$, for the inclusive and the high-energy event samples. The systematic errors do not include the uncertainty on the luminosity measurement. In the case of Bhabha scattering, both leptons have to be inside $44^\circ < \theta < 136^\circ$. The results for the 161–172 GeV data have been taken from Reference [2] and corrected using ZFITTER (s-channel processes) and BHAGENE (Bhabha scattering) to correspond to the kinematic cuts described in the text.

$\sqrt{s}$ (GeV)	inclusive N_f	N_b	A_fb	$A_\mathrm{fb}^\mathrm{SM}$	high energy N_f	N_b	A_fb	$A_\mathrm{fb}^\mathrm{SM}$
$\mathbf{e^+e^- \to \mu^+\mu^-(\gamma)}$								
130.0	61	29	$0.46 \pm 0.13 \pm 0.03$	0.324	38	5	$0.67^{+0.08}_{-0.11} \pm 0.02$	0.707
135.9	47	22	$0.44 \pm 0.15 \pm 0.04$	0.324	29	4	$0.75^{+0.06}_{-0.11} \pm 0.05$	0.686
161.3	35	21	$0.32^{+0.12}_{-0.14} \pm 0.05$	0.325	22	8	$0.59^{+0.13}_{-0.17} \pm 0.05$	0.619
172.1	23	16	$0.19^{+0.16}_{-0.17} \pm 0.05$	0.319	15	9	$0.31^{+0.18}_{-0.21} \pm 0.05$	0.598
182.7	133	59	$0.45 \pm 0.10 \pm 0.04$	0.313	86	23	$0.62^{+0.07}_{-0.09} \pm 0.02$	0.582
188.7	537	320	$0.30 \pm 0.04 \pm 0.02$	0.310	312	91	$0.58 \pm 0.04 \pm 0.02$	0.573
$\mathbf{e^+e^- \to \tau^+\tau^-(\gamma)}$								
130.1	36	17	$0.42 \pm 0.17 \pm 0.03$	0.324	22	3	$0.78^{+0.10}_{-0.16} \pm 0.02$	0.707
136.1	26	10	$0.53 \pm 0.22 \pm 0.01$	0.325	18	2	$0.96^{+0.10}_{-0.17} \pm 0.03$	0.686
161.3	15	12	$0.19^{+0.19}_{-0.20} \pm 0.10$	0.325	12	4	$0.97^{+0.03}_{-0.23} \pm 0.10$	0.619
172.1	16	16	$0.10^{+0.18}_{-0.19} \pm 0.10$	0.319	9	7	$0.18^{+0.25}_{-0.27} \pm 0.10$	0.598
182.7	96	52	$0.26 \pm 0.10 \pm 0.01$	0.313	62	29	$0.53^{+0.10}_{-0.11} \pm 0.03$	0.582
188.7	275	144	$0.23 \pm 0.06 \pm 0.02$	0.310	177	72	$0.44 \pm 0.06 \pm 0.02$	0.573
$\mathbf{e^+e^- \to e^+e^-(\gamma)}$								
130.0	214	44	$0.699 \pm 0.047 \pm 0.005$	0.715	201	27	$0.806 \pm 0.043 \pm 0.006$	0.799
136.1	199	29	$0.791 \pm 0.044 \pm 0.005$	0.728	185	17	$0.879 \pm 0.039 \pm 0.006$	0.804
161.3	240	43	$0.767 \pm 0.049 \pm 0.012$	0.762	206	29	$0.818 \pm 0.046 \pm 0.012$	0.809
172.1	203	51	$0.691 \pm 0.058 \pm 0.012$	0.771	176	31	$0.795 \pm 0.056 \pm 0.012$	0.812
182.7	1020	207	$0.728 \pm 0.021 \pm 0.004$	0.773	972	162	$0.778 \pm 0.021 \pm 0.004$	0.813
188.7	3045	546	$0.777 \pm 0.012 \pm 0.007$	0.779	2912	443	$0.819 \pm 0.012 \pm 0.003$	0.815

Table 3: Number of forward, N_f, and backward events, N_b, forward-backward asymmetries, A_fb, statistical and systematic errors and the Standard Model predictions, $A_\mathrm{fb}^\mathrm{SM}$, of the reactions $\mathrm{e^+e^-} \to \mu^+\mu^-(\gamma)$, $\mathrm{e^+e^-} \to \tau^+\tau^-(\gamma)$ and $\mathrm{e^+e^-} \to \mathrm{e^+e^-}(\gamma)$ for the inclusive and the high-energy event samples. In the case of Bhabha scattering, both leptons have to be inside $44^\circ < \theta < 136^\circ$. The results for the 161–172 GeV data have been taken from Reference [2] and corrected using ZFITTER (s-channel processes) and BHAGENE (Bhabha scattering) to correspond to the kinematic cuts described in the text.

$\cos\theta$ range	182.7 GeV			188.7 GeV		
	$\mu^+\mu^-(\gamma)$	$\tau^+\tau^-(\gamma)$	SM	$\mu^+\mu^-(\gamma)$	$\tau^+\tau^-(\gamma)$	SM
$\sqrt{s'} > 75$ GeV						
[-0.90,-0.70]	0.339±0.172	0.491±0.218	0.584	0.541±0.093	0.578±0.126	0.542
[-0.70,-0.50]	0.261±0.101	0.390±0.157	0.452	0.503±0.070	0.517±0.099	0.417
[-0.50,-0.30]	0.508±0.131	0.577±0.178	0.446	0.486±0.070	0.467±0.093	0.411
[-0.30,-0.10]	0.242±0.112	0.753±0.199	0.490	0.355±0.070	0.383±0.084	0.450
[-0.10, 0.10]	0.867±0.228	0.559±0.166	0.567	0.452±0.081	0.432±0.088	0.519
[0.10, 0.30]	0.443±0.143	0.461±0.155	0.677	0.740±0.087	0.619±0.098	0.620
[0.30, 0.50]	1.315±0.215	0.743±0.186	0.825	0.693±0.087	0.687±0.102	0.757
[0.50, 0.70]	0.769±0.161	0.853±0.200	1.035	1.004±0.101	0.916±0.117	0.950
[0.70, 0.90]	1.005±0.289	1.868±0.393	1.391	1.110±0.124	0.946±0.165	1.280
$\sqrt{s'} > 0.85\sqrt{s}$						
[-0.90,-0.70]	0.115±0.101	0.103±0.098	0.105	0.008±0.037	0.121±0.055	0.102
[-0.70,-0.50]	0.057±0.044	0.092±0.065	0.113	0.160±0.036	0.161±0.043	0.108
[-0.50,-0.30]	0.139±0.066	0.209±0.087	0.142	0.138±0.034	0.177±0.045	0.134
[-0.30,-0.10]	0.080±0.049	0.328±0.108	0.191	0.111±0.032	0.145±0.042	0.179
[-0.10, 0.10]	0.396±0.127	0.272±0.101	0.262	0.193±0.050	0.228±0.055	0.243
[0.10, 0.30]	0.190±0.078	0.255±0.099	0.353	0.393±0.056	0.328±0.061	0.326
[0.30, 0.50]	0.703±0.139	0.375±0.119	0.464	0.383±0.056	0.382±0.067	0.429
[0.50, 0.70]	0.427±0.111	0.529±0.143	0.597	0.521±0.066	0.460±0.075	0.551
[0.70, 0.90]	0.415±0.164	1.079±0.299	0.752	0.569±0.079	0.450±0.113	0.694

Table 4: Cross sections (in pb) for the processes $e^+e^- \to \mu^+\mu^-(\gamma)$ and $e^+e^- \to \tau^+\tau^-(\gamma)$ at 183 GeV and 189 GeV in bins of $\cos\theta$, compared to their Standard Model predictions. Statistical and systematic uncertainties are combined.

$\cos\theta$ range	182.7 GeV	SM	188.7 GeV	SM
[-0.719,-0.575]	0.404±0.157	0.306	0.167±0.075	0.290
[-0.575,-0.432]	0.306±0.115	0.352	0.300±0.065	0.344
[-0.432,-0.288]	0.532±0.127	0.433	0.526±0.070	0.395
[-0.288,-0.144]	0.539±0.122	0.532	0.524±0.067	0.488
[-0.144, 0.000]	0.930±0.153	0.712	0.708±0.075	0.664
[0.000, 0.144]	0.930±0.153	1.028	0.973±0.087	0.956
[0.144, 0.288]	1.638±0.199	1.609	1.405±0.103	1.509
[0.288, 0.432]	2.779±0.259	2.810	2.561±0.139	2.607
[0.432, 0.575]	5.025±0.347	5.350	5.054±0.194	5.003
[0.575, 0.719]	12.39±0.54	11.91	11.23±0.29	11.16

Table 5: Cross sections (in pb) for $\zeta < 25^\circ$ for the process $e^+e^- \to e^+e^-(\gamma)$ at 183 GeV and 189 GeV in bins of $\cos\theta$, compared to their Standard Model predictions. Statistical and systematic uncertainties are combined.

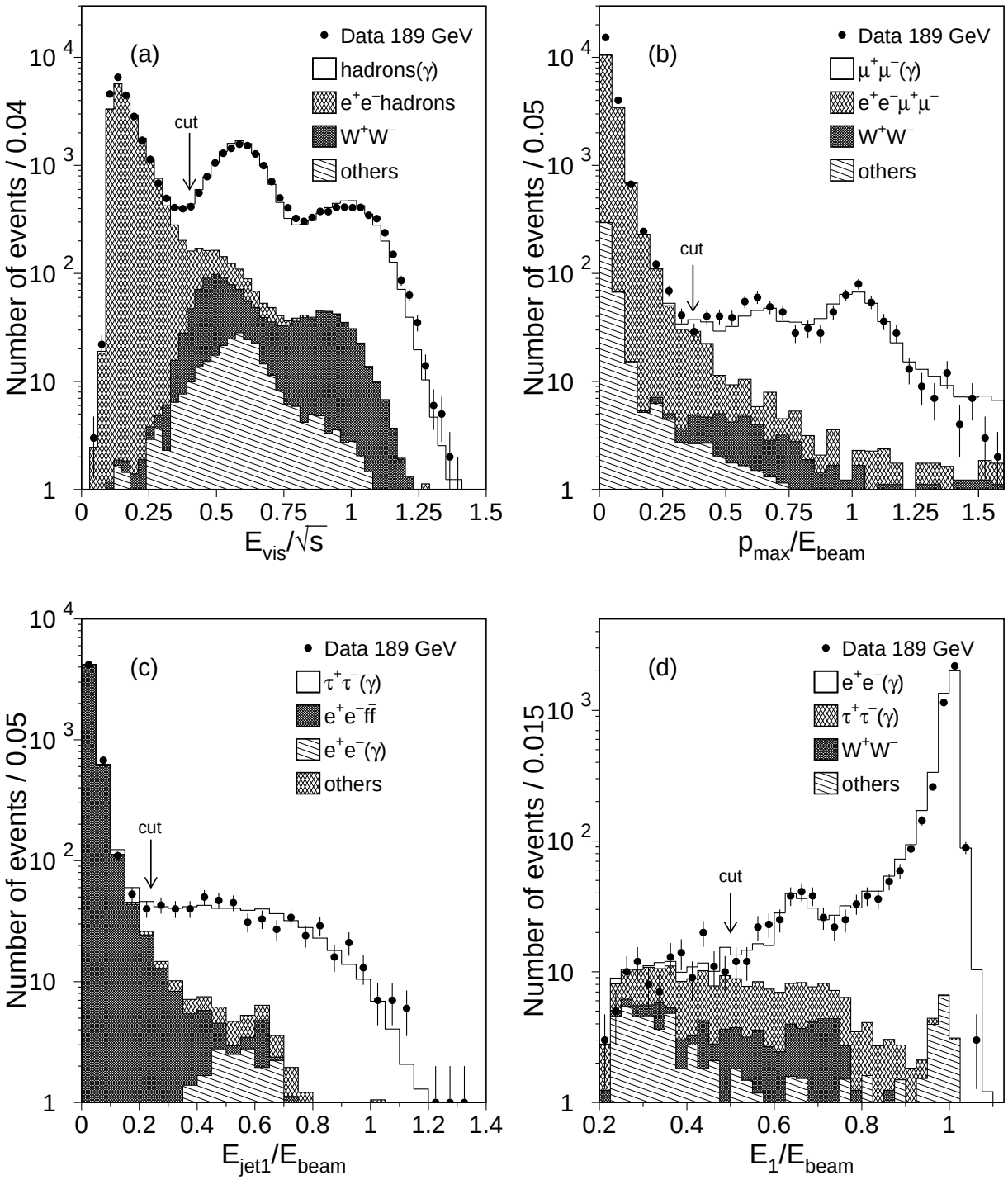

Figure 1: (a) The total visible energy normalised to the centre-of-mass energy, $\sqrt{s}$, for the selection of $e^+e^- \to$ hadrons(γ) events, (b) highest muon momentum normalised to the beam energy for the selection of $e^+e^- \to \mu^+\mu^-(\gamma)$ events, (c) highest tau jet energy normalised to the beam energy for the selection of $e^+e^- \to \tau^+\tau^-(\gamma)$ events, and (d) highest electron energy normalised to the beam energy for the selection of $e^+e^- \to e^+e^-(\gamma)$ events.

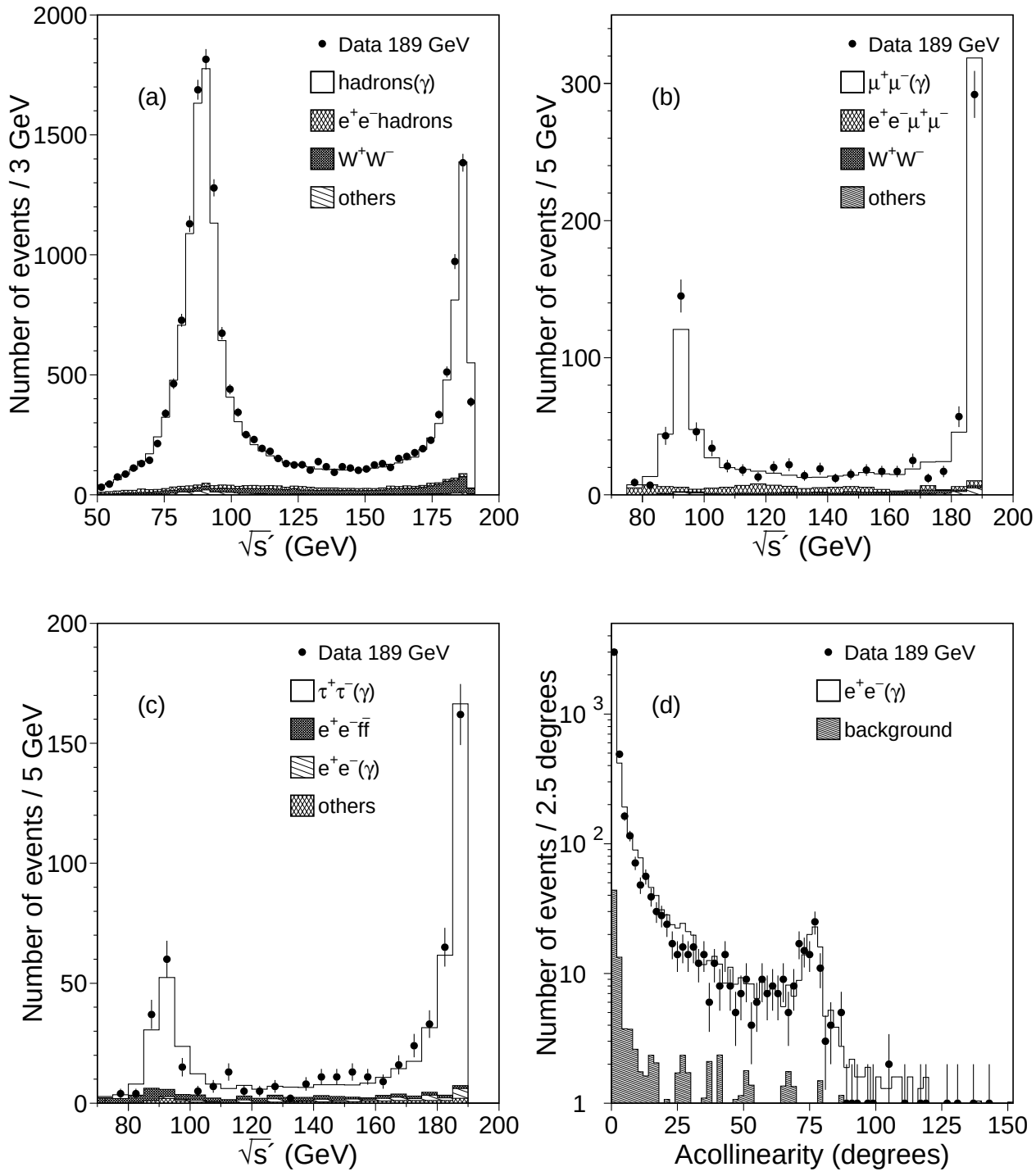

Figure 2: The reconstructed effective centre-of-mass energy, $\sqrt{s'}$, for the selection of (a) $e^+e^- \to$ hadrons(γ) events, (b) $e^+e^- \to \mu^+\mu^-(\gamma)$ events, (c) $e^+e^- \to \tau^+\tau^-(\gamma)$ events, and the reconstructed acollinearity angle for (d) $e^+e^- \to e^+e^-(\gamma)$ events.

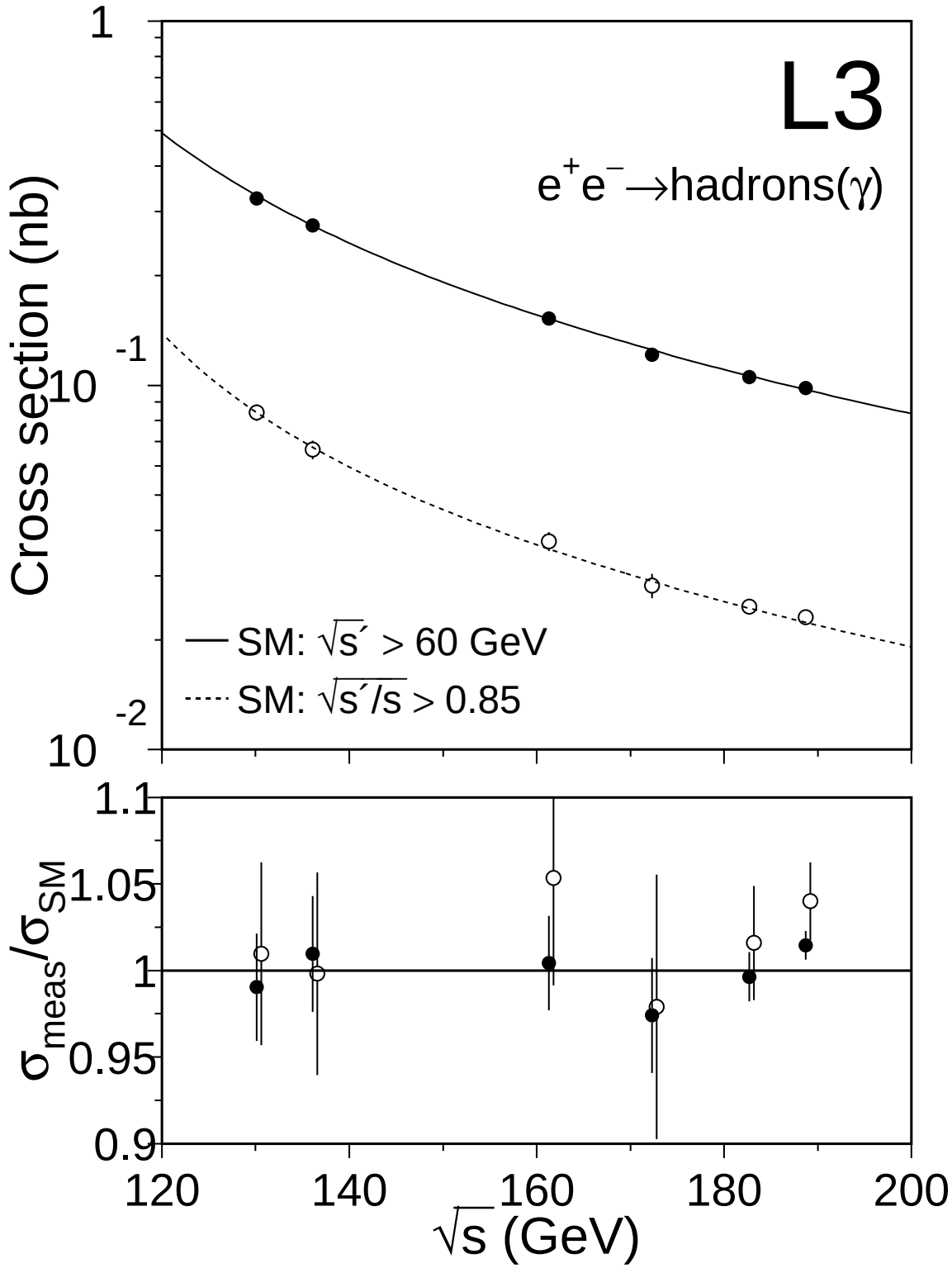

Figure 3: Cross sections of the process $e^+e^- \rightarrow$ hadrons(γ), for the inclusive (solid symbols) and the high-energy sample (open symbols). The Standard Model predictions are shown as a solid line for the inclusive sample and as a dashed line for the high-energy sample. The lower plot shows the ratio of measured and predicted cross sections.

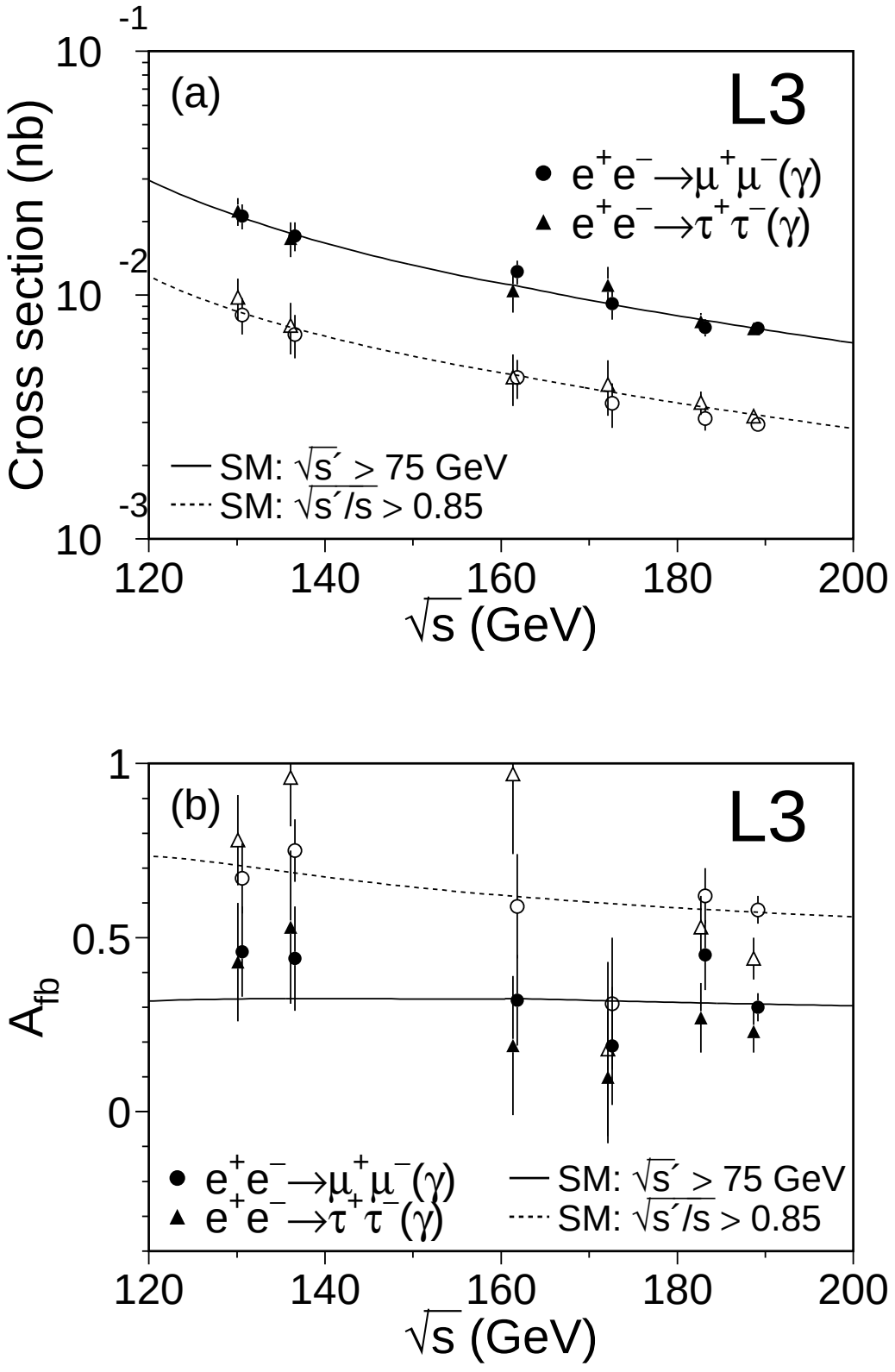

Figure 4: Cross sections (a) and forward-backward asymmetries (b) of the processes $e^+e^- \to \mu^+\mu^-(\gamma)$ and $e^+e^- \to \tau^+\tau^-(\gamma)$ for the inclusive (solid symbols) and the high-energy sample (open symbols). The Standard Model predictions are shown as a solid line for the inclusive sample and as a dashed line for the high-energy sample.

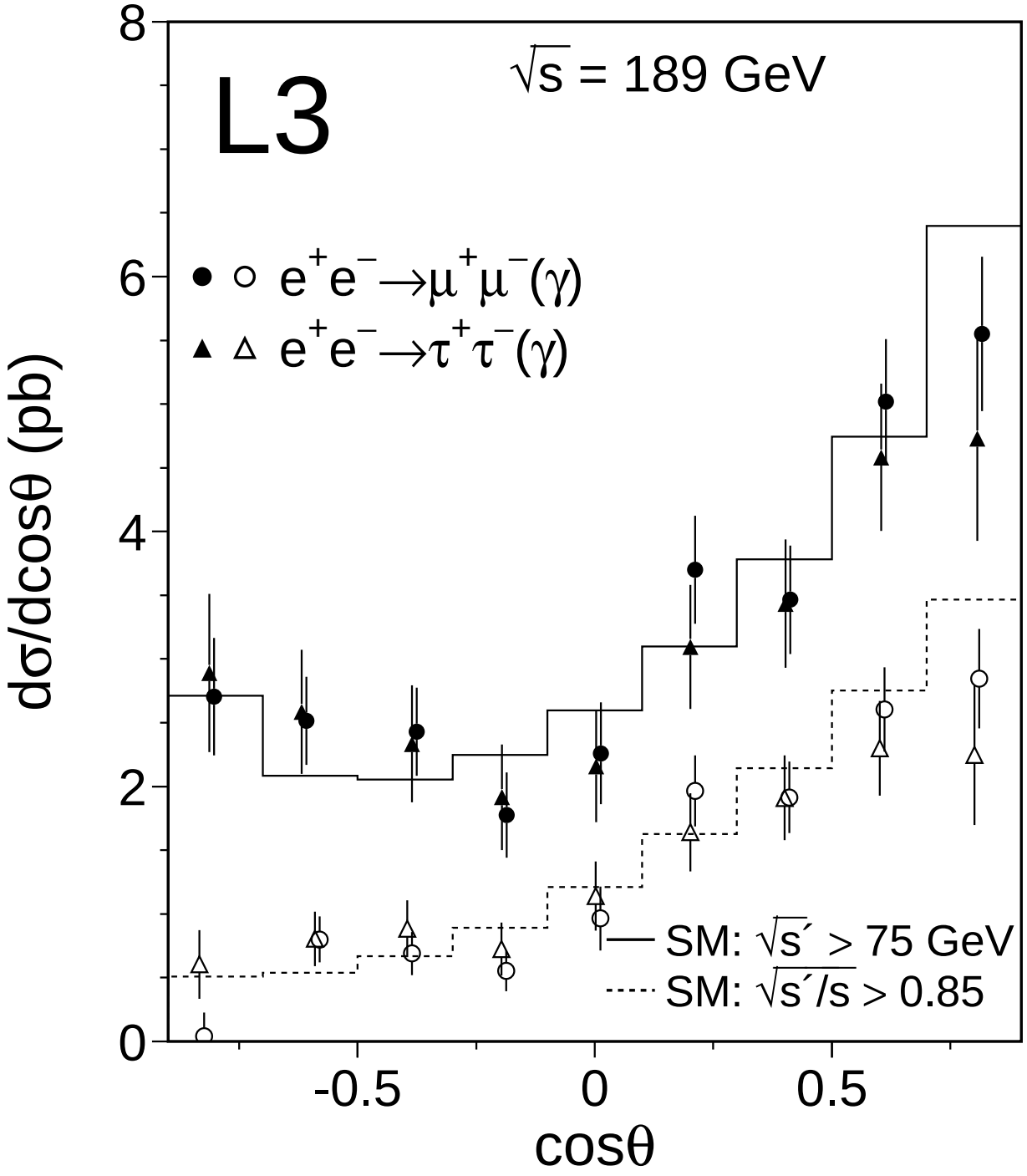

Figure 5: Differential cross section for the inclusive (solid symbols) and high-energy (open symbols) event samples, for the processes $e^+e^- \to \mu^+\mu^-(\gamma)$ and $e^+e^- \to \tau^+\tau^-(\gamma)$ at $\sqrt{s} = 189$ GeV. The lines indicate the Standard Model predictions.

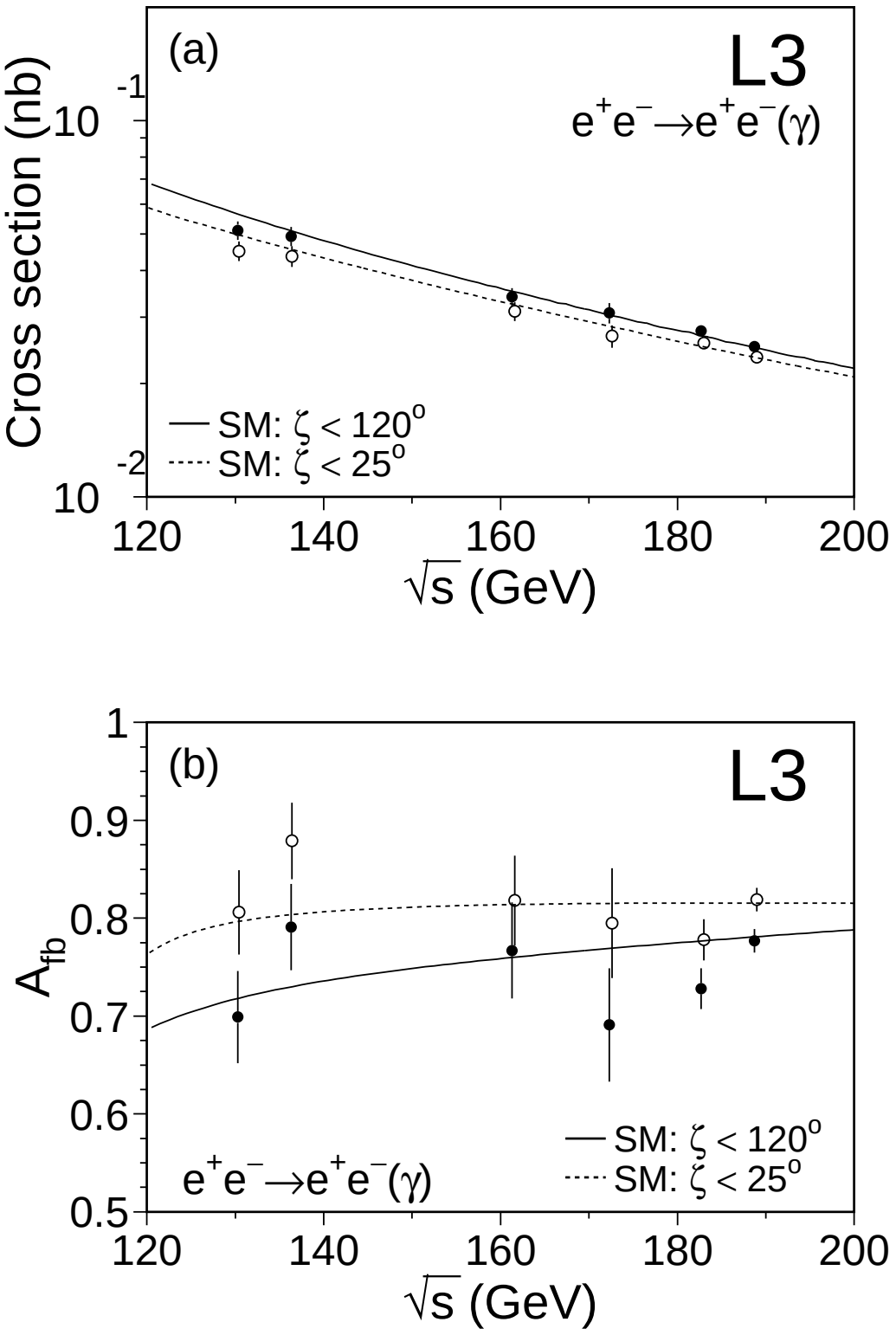

Figure 6: Cross sections (a) and forward-backward asymmetries (b) of the process $e^+e^- \to e^+e^-(\gamma)$ for the inclusive (solid symbols) and the high-energy sample (open symbols). The Standard Model predictions are shown as a solid line for the inclusive sample and as a dashed line for the high-energy sample. The two electrons are required to be inside $44^\circ < \theta < 136^\circ$.

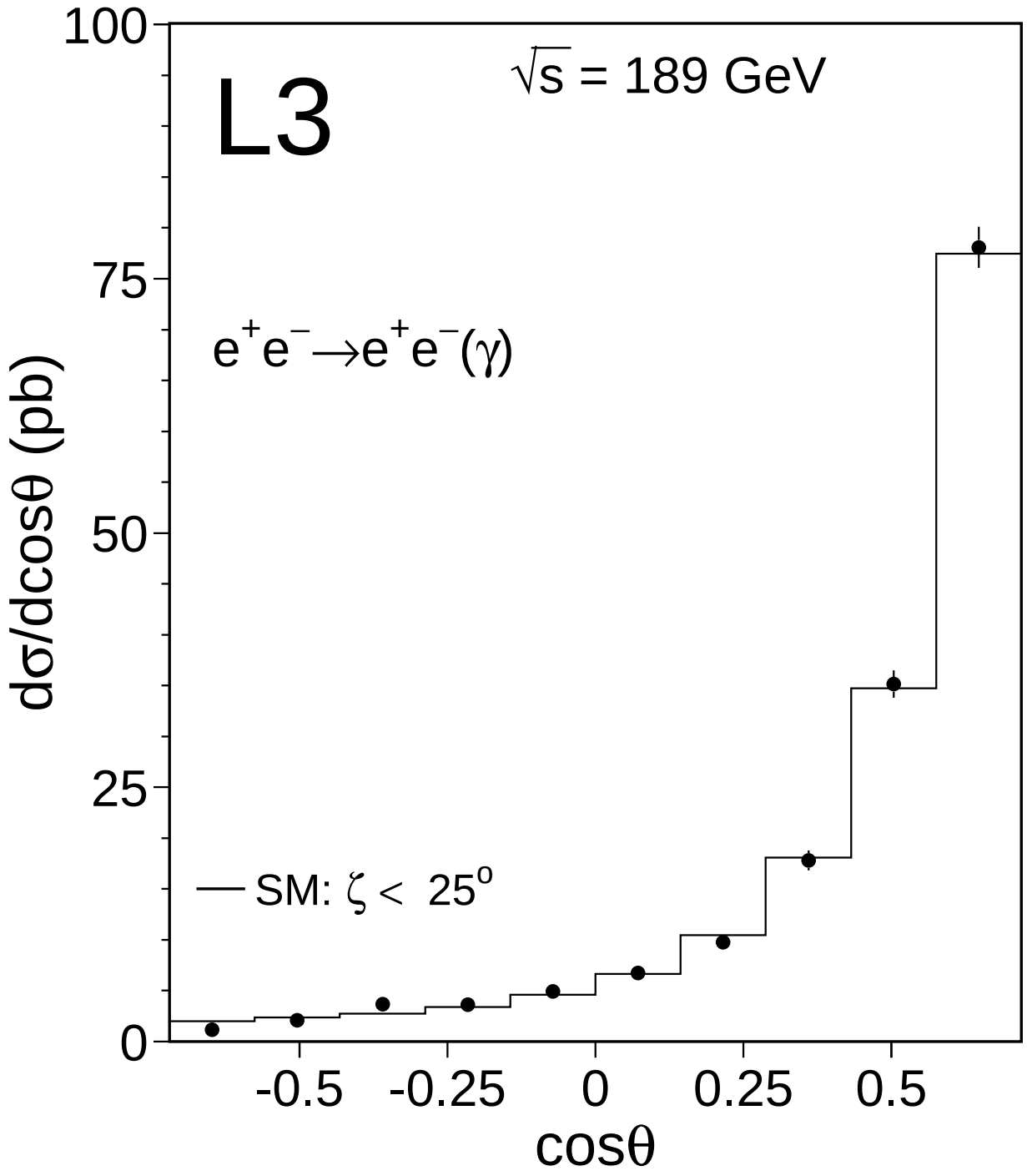

Figure 7: Differential cross section for the high-energy event sample, for the process $e^+e^- \to e^+e^-(\gamma)$ at $\sqrt{s} = 189$ GeV. The line indicates the Standard Model prediction.